RESEARCH ARTICLE

124I-Iodo-DPA-713 Positron Emission Tomography in a Hamster Model of SARS-CoV-2 Infection

Camilo A. Ruiz-Bedoya[1,2,3], Filipa Mota[1,2,3], Alvaro A. Ordonez[1,2,3], Catherine A. Foss[1,4], Alok K. Singh[3], Monali Praharaj[5], Farina J. Mahmud[1,2,3], Ali Ghayoor[6], Kelly Flavahan[1,2,3], Patricia De Jesus[1,2,3], Melissa Bahr[1,2,3], Santosh Dhakal[7], Ruifeng Zhou[7], Clarisse V. Solis[8], Kathleen R. Mulka[8], William R. Bishai[3], Andrew Pekosz[7,8], Joseph L. Mankowski[8], Jason Villano[8], Sabra L. Klein[7], and Sanjay K. Jain[1,2,3,4]

[1]Center for Infection and Inflammation Imaging Research, Johns Hopkins University School of Medicine, Baltimore, MD, USA

[2]Department of Pediatrics, Johns Hopkins University School of Medicine, 1550 Orleans Street, CRB-II Room 109, Baltimore, MD, USA

[3]Center for Tuberculosis Research, Johns Hopkins University School of Medicine, Baltimore, MD, USA

[4]Russell H. Morgan Department of Radiology and Radiological Sciences, Johns Hopkins University School of Medicine, Baltimore, MD, USA

[5]Bloomberg-Kimmel Institute for Immunotherapy, Johns Hopkins University School of Medicine, Baltimore, MD, USA

[6]Invicro, Boston, MA, USA

[7]W. Harry Feinstone Department of Molecular Microbiology and Immunology, The Johns Hopkins Bloomberg School of Public Health, Baltimore, MD, USA

[8]Department of Molecular and Comparative Pathobiology, Johns Hopkins University School of Medicine, Baltimore, MD, USA 2021

Abstract

Purpose: Molecular imaging has provided unparalleled opportunities to monitor disease processes, although tools for evaluating infection remain limited. Coronavirus disease (COVID-19) caused by severe acute respiratory syndrome coronavirus 2 (SARS-CoV-2) is mediated by lung injury that we sought to model. Activated macrophages/phagocytes have an important role in lung injury, which is responsible for subsequent respiratory failure and death. We performed pulmonary PET/CT with 124I-iodo-DPA-713, a low-molecular-weight pyrazolopyrimidine ligand selectively trapped by activated macrophages cells, to evaluate the local immune response in a hamster model of SARS-CoV-2 infection.

Procedures: Pulmonary 124I-iodo-DPA-713 PET/CT was performed in SARS-CoV-2-infected golden Syrian hamsters. CT images were quantified using a custom-built lung segmentation tool. Studies with DPA-713-IRDye680LT and a fluorescent analog of DPA-713 as well as histopathology and flow cytometry were performed on post-mortem tissues.

Results: Infected hamsters were imaged at the peak of inflammatory lung disease (7 days post-infection). Quantitative CT analysis was successful for all scans and demonstrated worse pulmonary disease in male versus female animals ($P < 0.01$). Increased 124I-iodo-DPA-713 PET activity co-localized with the pneumonic lesions. Additionally, higher pulmonary 124I-iodo-DPA-713 PET activity was noted in male versus female hamsters ($P = 0.02$). DPA-713-IRDye680LT also localized to the pneumonic lesions. Flow cytometry demonstrated a higher percentage of myeloid and CD11b + cells (macrophages, phagocytes) in male versus female lung tissues ($P = 0.02$).

Conclusion: [124]I-Iodo-DPA-713 accumulates within pneumonic lesions in a hamster model of SARS-CoV-2 infection. As a novel molecular imaging tool, [124]I-Iodo-DPA-713 PET could serve as a noninvasive, clinically translatable approach to monitor SARS-CoV-2-associated pulmonary inflammation and expedite the development of novel therapeutics for COVID-19.

Introduction

Compared with conventional technologies currently utilized to investigate the pathogenesis of infectious diseases, imaging can evaluate disease processes deep within the body noninvasively and relatively rapidly. Tomographic imaging can provide whole-body, three-dimensional assessments, enabling a complete view of the disease process, which is less affected by sampling bias (e.g., with biopsy or resected tissues). Molecular imaging can also provide detailed spatiotemporal visualization of molecular events noninvasively and longitudinally in the same individual [1]. While continued advances in molecular imaging have provided unparalleled opportunities to monitor disease progression in oncology and neurology, their application for the evaluation of infections remains limited.

Coronavirus disease (COVID-19), caused by severe acute respiratory syndrome coronavirus 2 (SARS-CoV-2), has affected over 191 million people worldwide and led to over 4 million deaths. Severe COVID-19 is worse for males than females [2] and can lead to dysregulated inflammation through the activation of pro-inflammatory pathways and recruitment of immune cells leading to lung disease [3]. While the incidence of COVID-19 is similar between the sexes, adult males are almost 3 times more likely to be admitted into ICUs and twice as likely to die as females [4, 5]. Therefore, understanding the inflammatory and immunological responses to SARS-CoV-2 infection is fundamental and could assist in the development of novel therapeutic interventions. The golden Syrian hamster (*Mesocricetus auratus*) inoculated with SARS-CoV-2 develops pulmonary disease, including bilateral and peripherally distributed regions of lung consolidation which can be assessed with computed tomography (CT) [6, 7] with infiltration by myeloid cells (neutrophils, monocytes, and macrophages) at infection sites

[8]. Adult male golden Syrian hamsters also develop worse morbidity and pulmonary disease than females [9]. Here, we evaluated [124]I-iodo-DPA-713 PET/CT as a noninvasive molecular imaging tool to detect pulmonary inflammation in SARS-CoV-2-infected hamsters. Radioiodinated DPA-713, which targets the translocator protein (TSPO), a mitochondrial protein upregulated in activated macrophages/phagocytic cells, has been utilized to image pulmonary infections and inflammatory diseases [10]. Recently, [124]I-iodo-DPA-713 PET has also been translated to the clinic [11].

Materials and Methods

Ethics

All animal protocols were approved by the Johns Hopkins University Biosafety, Radiation Safety, and Animal Care and Use Committees.

Viral Propagation

VeroE6-TMPRSS2 cells (National Institute of Infectious Diseases, Japan) were cultured at 37 °C with 5% CO_2 in Dulbecco's Modified Eagle Medium (DMEM) supplemented with 10% fetal bovine serum, and 100 units/ml of penicillin–streptomycin. The SARS-CoV-2/USA-WA1/2020, NR-52281 isolate was obtained from BEI Resources (National Institutes of Allergy and Infectious Diseases). Infectious stocks were grown by infecting VeroE6-TMPRSS2 cells and collecting supernatant upon observation of cytopathic effect; debris were removed by centrifugation and passage through a 0.22-μm filter (Sigma-Aldrich). The supernatant was then aliquoted and stored at −80 °C. Infectious virus titers were determined by tenfold serially diluting and plating the supernatant onto 96-well plates with monolayers of Vero E6-TMPRSS2 cells in replicates of six for 5 days at 37 °C. Incubation was followed by fixation with 4% formaldehyde, staining with naphthol blue-black solution, and scoring of cytopathic effects.

Animal Studies

Golden Syrian hamsters (male and female, 6–8 weeks old; Envigo, Indianapolis, IN) with surgically implanted central venous catheters were utilized. The animals were housed individually with ad libitum access to food, water, and cage enrichment. After 1 week of acclimatization in the animal biosafety level-3 (ABSL-3) facility, the animals were anesthetized with ketamine and xylazine for intranasal infection with 1.5×10^5 50% tissue culture infectious dose ($TCID_{50}$) of SARS-CoV-2, delivered in 100 μL of DMEM.

Imaging

[124]I-iodo-DPA-713 was synthesized in-house as described previously yielding > 90% radiochemical purity [12].

Fig. 1 Experimental scheme. **a** Golden Syrian hamsters were intranasally challenged with SARS-CoV-2 and imaging performed as outlined. **b** In-house developed, transparent, and sealed biocontainment cells with 0.02-μm filters attached to the inlet and outlet for O₂ and anesthesia and compliant with BSL-3 containment. **c** SARS-CoV-2-infected hamster inside a biocontainment bed being imaged at Ci3R imaging facility (Johns Hopkins University).
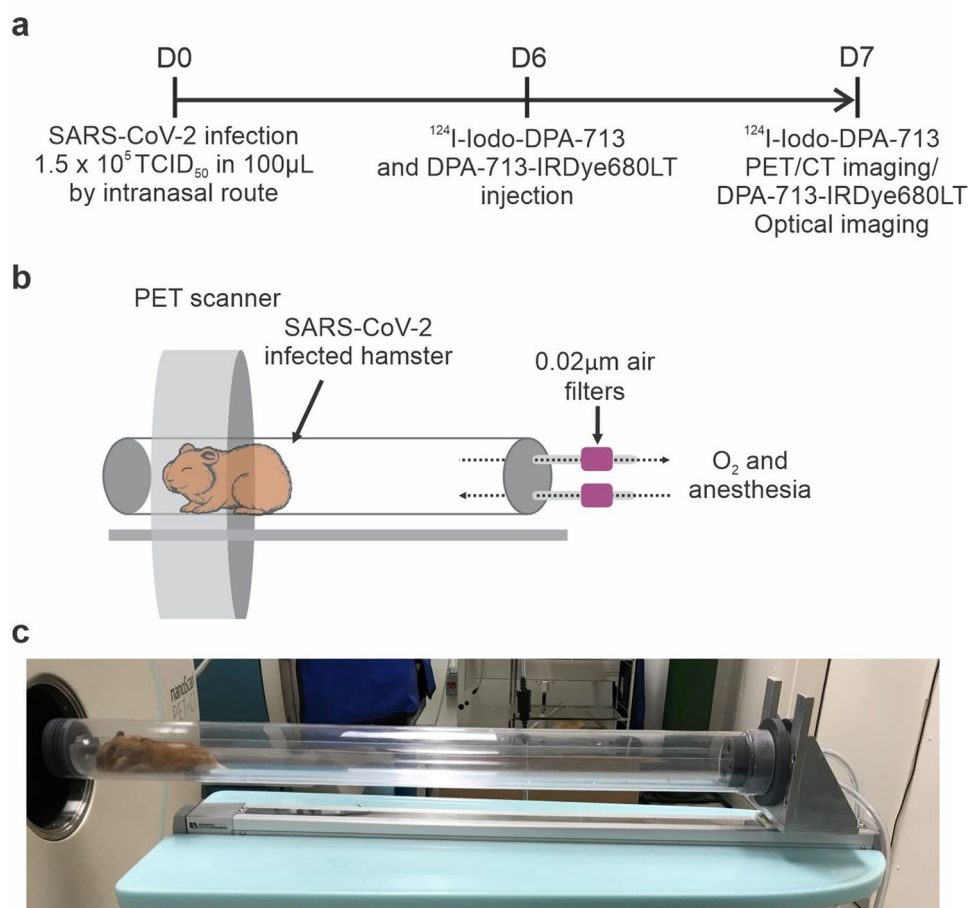
SARS-CoV-2-infected hamsters ($n = 3$ male, $n = 4$ female) underwent PET/CT at 7 days post-infection, and 24 h after intravenous administration of ^{124}I-iodo-DPA-713 (10.22 ± 0.14 MBq/hamster) via the surgically implanted central venous catheter (Fig. 1a). A 20-min PET acquisition and subsequent CT were performed using the nanoScan PET/CT (Mediso, Arlington, VA). An additional set of animals ($n = 15$ male, $n = 11$ female) underwent CT scans only [9, 13]. Given that SARS-CoV-2 is designated as a BSL-3 pathogen, live SARS-CoV-2-infected animals were imaged inside transparent and sealed biocontainment cells developed in-house, compliant with BSL-3 containment and capable of delivering air-anesthetic mixture to sustain live animals during imaging [13–15] (Fig. 1b, c). DPA-713-IRDye680LT, a fluorescent analog of DPA-713, was intravenously administered 24 h prior euthanasia. Lungs were collected, formalin-fixed, and imaged with the Peral® Impulse Imager (LI-COR, Lincoln, NE).

Lung Segmentation Tool and Image Analysis

A multi-atlas lung segmentation (MALS) algorithm was used to create the whole lung volumes of interest (VOI) [16, 17]. A reference library was generated from a selection of study images that included SARS-CoV-2-infected hamsters in various stages of lung disease. A bounding box for the lung VOI was generated using a combination of rigid and affine transformations followed by a high-dimensional deformable registration technique inside this bounding box to efficiently refine the linear mapping accuracy [18]. The propagated labels were merged using a weighted voting-based label fusion technique [19]. A local search algorithm was also used to improve robustness against registration errors [20]. Pulmonary lesions were defined using a global Hounsfield units (HU) threshold ≥ 0 [21]. The data are represented as CT score [(pulmonary lesions volume/whole lung volume)$\times 100$]. The investigators analyzing the CT were blinded to the group assignments.

VivoQuant™ 2020 (Invicro, Boston, MA, USA) was used for visualization and quantification. Scatter and attenuation corrections were applied to the PET data and multiple VOIs were manually drawn per animal using the CT as a reference.

Histopathology and Immunofluorescence

Formalin-fixed and paraffin-embedded tissue sections were stained with hematoxylin and eosin (H&E) or anti-Iba-1 antibody (Wako; 019–19,741 Richmond, VA; at a dilution of 1:2000). Morphometric analyses were performed on affected lung tissues using Image J software (NIH, USA) [22]. A minimum of three fields of view were obtained from each animal ($n = 6$ animals; 3 male and 3 female hamsters). Heat-induced

epitope retrieval was conducted by heating slides to 95 °C for 20 min in sodium citrate–based ER1 buffer (Leica Biosystems, Richmond, IL) before immunostaining. Immunostaining was performed using the Bond RX automated system (Leica Biosystems, Richmond, IL). Positive immunostaining was visualized using diaminobenzidine tetrahydrochloride (DAB) and slides were counterstained with hematoxylin.

Flow Cytometry

Lungs were harvested and homogenized, the cells filtered and washed with PBS followed by RBC lysis [23]. Cell viability was determined with trypan blue dye staining. A single-cell suspension was stained with Zombie Aqua Fixable Viability Kit (Biolegend), resuspended in FACS buffer (1% bovine serum albumin in saline), and incubated in block buffer prior to surface staining with anti-CD11b antibody (Novus Biologicals, #NB110-89474PECY7, polyclonal) for macrophages, monocytes, and granulocytes. Cells were fixed using intracellular fixation buffer and data acquired and analyzed using FACSDiva software and FlowJo (v10). The gating strategy is reported in Figure S1. Myeloid and lymphoid cells were identified based on their scatter characteristics.

Virus Titration and Anti-spike Receptor-Binding Domain IgG ELISA

All procedures handling live virus were performed in a biosafety level-3 (BSL-3) facility. The $TCID_{50}$ of the virus in the supernatant and lung tissues was calculated using the Reed-Muench method [9]. Hamster antibody titers from plasma were performed using ELISA protocols adapted from human COVID-19 antibody assays described previously [9, 24]. Briefly, ELISA plates (96-well plates, Immunol 4HBX, Thermo Fisher Scientific) were coated with anti-spike receptor-binding domain (S-RBD). An HRP-conjugated secondary IgG (Abcam, MA, USA) was used with titer cutoff of three times the absorbance of first dilution of mock (uninfected) animal samples.

Statistical Analysis

The data are represented on a linear scale as median and interquartile range (IQ). Statistical comparisons were performed using a two-tailed Mann–Whitney U test. P values of < 0.05 were considered statistically significant. All statistical analyses were performed using Prism 8 (GraphPad Software, San Diego, CA, USA).

Results

Lung Pathology in SARS-CoV-2

Seven days post-infection, pulmonary CT demonstrated extensive peripheral, bilateral, and multi-lobular ground-glass opacities (GGO), and mixed GGO with consolidation (Figure S2). Lungs were examined after necropsy showing focal areas of spotted brown coloration distributed around all lobules. Histopathology findings were consistent with previous reports [7, 25], showing multiple areas of consolidation characterized by abundant infiltration of inflammatory cells of predominantly macrophages, intermixed with neutrophils and lymphocytes, as well as type II pneumocyte hyperplasia and multinucleated cells (Fig. 2a). To reduce bias in the visual assessment of lung disease, a custom-built lung segmentation tool was utilized to quantify pathology of the whole lung on chest CT (Fig. 2b and Movie S1). Our segmentation tool allowed a semi-automated quantification of the lung volume and determined regions of increased tissue density (HU > 0). Quantitative CT analysis was performed for all scans with an average total lung volume of 2.1 ± 0.3 mL. While the whole lung volume was similar between sexes ($P = 0.83$), the CT score (disease severity) was higher in males compared to females ($P < 0.01$) (Fig. 2d). Additionally, no difference were noted in the CT score (disease severity) in males compared to females in uninfected hamsters (Figure S3).

^{124}I-Iodo-DPA-713 PET/CT

Whole-body ^{124}I-iodo-DPA-713 PET/CT of a representative SARS-CoV-2 hamster is shown (Figure S4a-b). As previously reported in other mammalian species [11, 20, 26], ^{124}I-iodo-DPA-713 followed urinary and hepatobiliary excretion, with the signal localizing to the liver, gastrointestinal tract, and kidneys. Specific uptake in macrophage-rich brown fat and metabolized iodine in the thyroid was also noted, with minimal PET activity in the brain parenchyma. In the lungs, ^{124}I-iodo-DPA-713 PET signal co-localized with the pneumonic lesions noted on the CT (Fig. 3a) and quantification of the signal demonstrated that ^{124}I-iodo-DPA-713 uptake was higher in the pneumonic regions, compared to the unaffected areas of the lung ($P < 0.01$) (Fig. 3b). Additionally, post-mortem analysis demonstrated that DPA-713-IRDye680LT fluorescence also co-localized with the pneumonic regions in the lung (Fig. 3c). ^{124}I-iodo-DPA-713 PET activity was significantly higher in males compared to females ($P < 0.05$) (Fig. 3d). However, no differences were noted in the ^{124}I-iodo-DPA-713 PET activity in males compared to females in unaffected areas of the lung (Figure S4c). Post-mortem analysis was consistent with imaging findings demonstrating worse lung disease in male versus female hamsters (Figure S5a). Immunostaining demonstrated a rich cluster of Iba-1 + macrophages within the consolidated areas in the lung parenchyma in both sexes at the peak of lung disease (7 days post-infection) (Fig. 4a). To characterize the immune response, multicolor flow-cytometric analyses were performed. The percentage of lung myeloid and specifically CD11b + cells (macrophages, phagocytes) was higher in male versus female animals ($P < 0.05$) (Fig. 4b). Conversely, the percentage of pulmonary lymphocytes was lower in males versus females ($P < 0.01$).
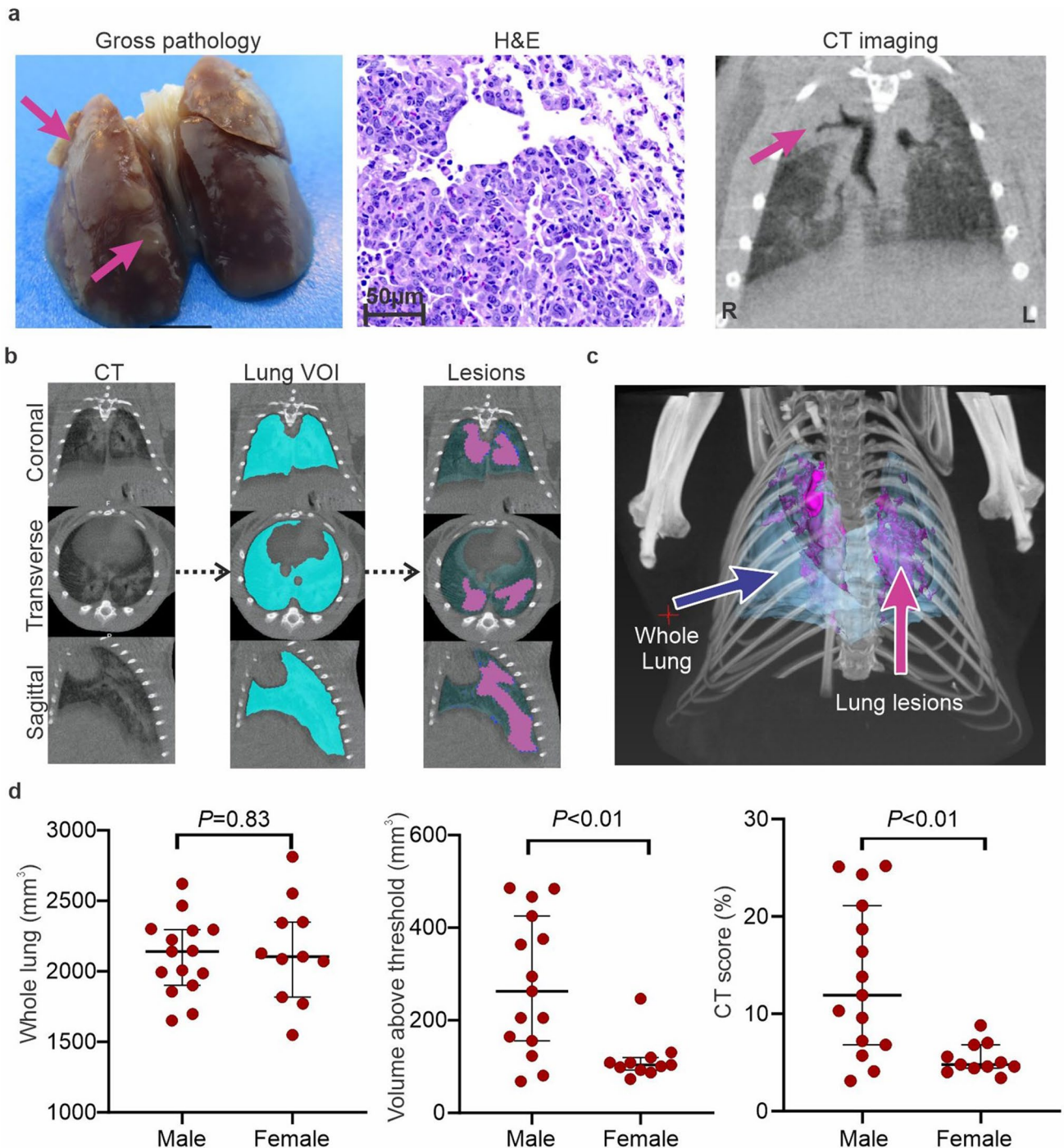
Fig. 2 Lung pathology in SARS-CoV-2-infected hamsters. **a**, Gross pathology, histopathology (H&E, 40×, scales bars of 50 μm), and CT findings at 7 days post-infection. Ground glass opacities (GGO) and consolidations were detected by CT scan (pink arrows indicates affected area). **b** Automated lung segmentation of CT images from a SARS-CoV-2-infected hamster is shown. **c** Maximum intensity projection of SARS-CoV-2-infected hamster demonstrating the lung (blue) and pneumonic areas (pink). **d** Whole lung, lung volume above threshold, and CT score for male ($n=15$) and female ($n=11$) hamsters. While no differences are noted in the whole lung volumes, the lung disease (CT score) was substantially worse in male compared to female animals. Data represented as median ± interquartile range.

To explore other biological differences during SARS-CoV-2 infection, antibody responses in plasma and viral titers in lungs were evaluated at the time of imaging (7 days post-infection). Anti-S-RBD IgG titers in plasma were noted between male and female hamsters and viral titers in the lungs were undetectable (Figure S5b-c). Both findings are consistent with previous reports at this time point after infection [9].

Fig. 3 Pulmonary [124]I-iodo-DPA-713 PET/CT of SARS-CoV-2-infected hamsters. **a** Transverse lung sections of a representative hamster imaged with [124]I-iodo-DPA-713 showing higher uptake within the GGO and pneumonic areas. **b** [124]I-iodo-DPA-713 PET activity is higher in pneumonic regions compared to unaffected lung. **c** DPA-713-IRDye680LT fluorescence co-localizes with the diseased lung. **d** [124]I-iodo-DPA-713 PET signal is higher in male versus female hamsters. A VOI was created for each lung lesion (GGO and consolidations) in males ($n=11$), females ($n=11$) and unnaffected lung ($n=19$). Data represented as median ± interquartile range.
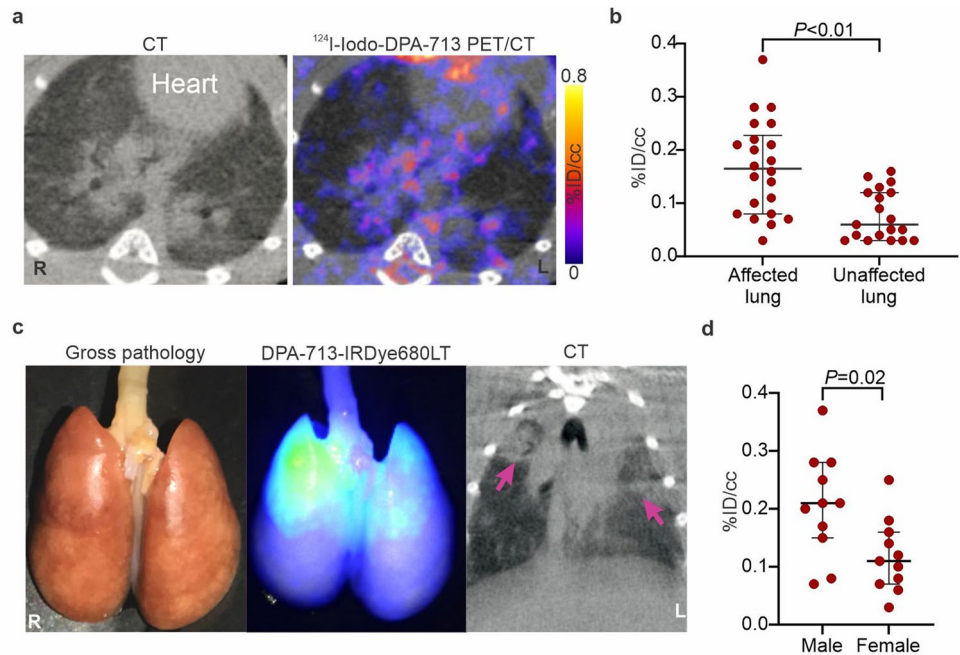
Discussion

There has been increasing interest in developing molecular imaging probes to assist in the diagnosis and management of infections [1, 27]. In COVID-19, findings from human autopsies, plasma, and bronchoalveolar lavage samples have demonstrated dysregulation of the myeloid compartment, peripheral lymphopenia, and neutrophil activation [3, 8, 28, 29]. SARS-CoV-2-infected golden Syrian hamsters develop mild-to-moderate clinical manifestations and recreate radiological and pathological features similar to those noted in human disease [9], with areas of consolidation and ground-glass opacities (GGO), and infiltration of neutrophil, monocytes, and macrophages in the lung [8]. Emerging literature also suggests that both the numbers and pro-inflammatory responses of lung monocytes and macrophages increase with disease severity [30]. Sex is a crucial variable that influences the innate and adaptive host immune responses to viruses [31] and there is substantial data demonstrating more severe disease in male versus female patients with COVID-19 [32–39] as well as hamster models [9].

Chest CT has been utilized in patients with SARS-CoV-2 for the diagnosis and monitoring of lung disease [40, 41]. Additionally, efforts are being made to develop artificial intelligence-enabled analysis of chest CT for rapid diagnosis of patients with COVID-19 [42, 43]. Prior studies with preclinical animal models of SARS-CoV-2 have relied on semiquantitative or non-automated methods to score disease severity on CT [7, 44]. We developed and utilized a semi-automated lung segmentation tool for rapid, reliable, and unbiased analysis of chest CT in SARS-CoV-2-infected hamsters. Our total lung volume data (without

positive pressure) is consistent with prior published data about lung volumes in hamsters [21, 45] and thus validates this technique. Moreover, similar to what has been reported in patients with COVID-19 [9, 34], male hamsters had worse pulmonary disease compared to females.

Radioiodinated DPA-713 has been validated in several animal models as a selective marker for activated macrophages/phagocytes, but not lymphoid cells [10, 12, 20, 26, 46, 47]. As a small molecular imaging probe, iodo-DPA-713 has an excellent pharmacokinetic profile with low background in pulmonary tissues [11, 20]. In this study, the in vivo biodistribution of [124]I-iodo-DPA-713 in hamsters was comparable to prior studies with other mammalian species, with slightly higher hepatobiliary elimination [11, 20, 26]. [124]I-Iodo-DPA-713 activity colocalized with the pulmonary infection sites and analysis disaggregated by sex demonstrated that male hamsters had higher PET activity compared to females. Post-mortem analysis using optical imaging and DPA-713-IRDye680LT confirmed these findings. Additionally, multicolor flow cytometry demonstrated that the lungs of male hamsters had a higher percentage of CD11b + myeloid cells (macrophages, phagocytes) versus females, but higher lymphocyte infiltration was detected in females, which is consistent with human studies [39, 48]. Given the limited availability of reagents, a more detailed flow cytometric analysis could not be performed. Finally, while the long physical half-life of I-124 allows for an ideal imaging time-point after tracer injection (typically > 4 h), other PET isotopes such as F-18, which provide higher positron yield, should be considered in the design of new tracers for these applications.
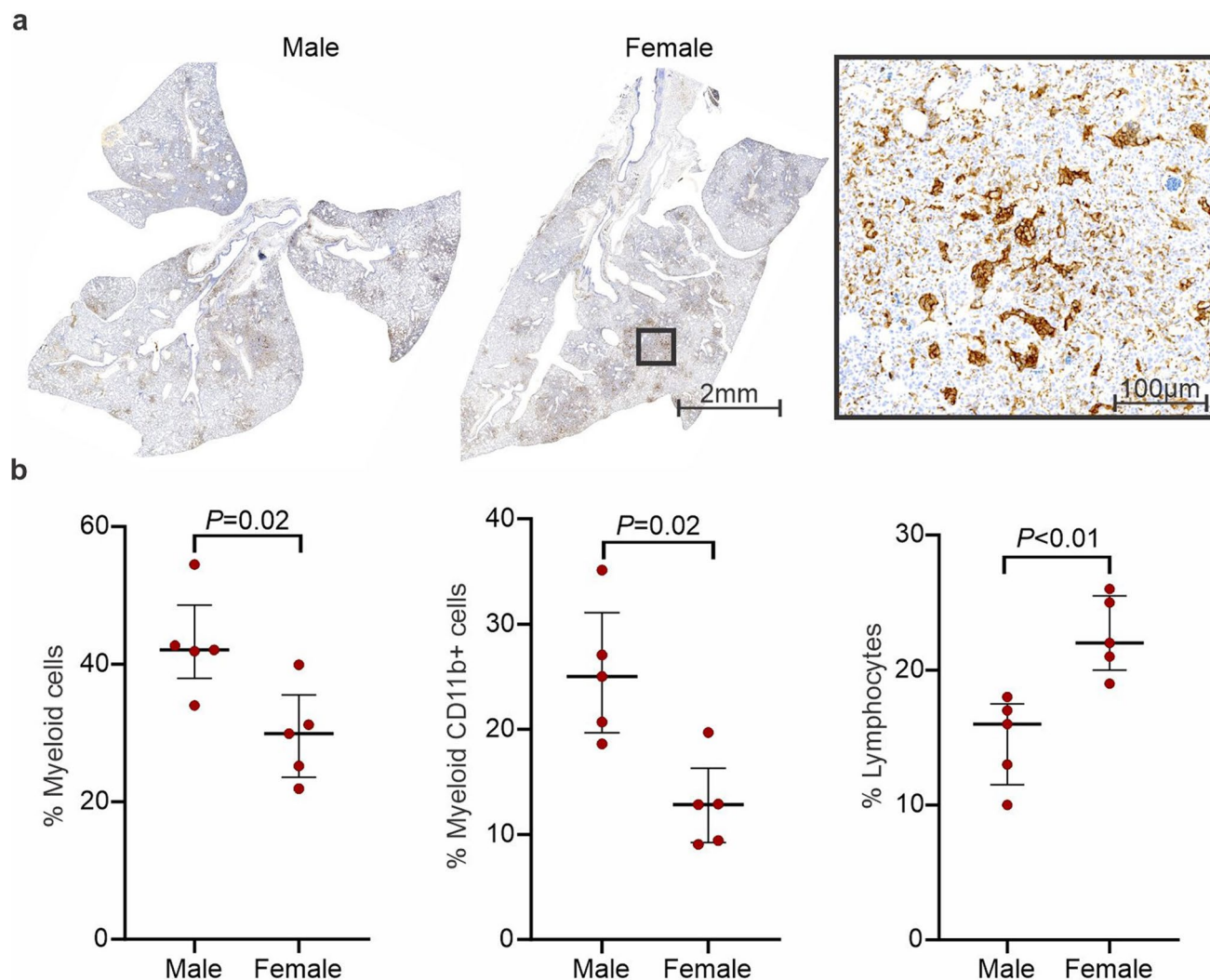
Fig. 4 Iba-1 staining and flow cytometry. **a** Immunohistochemistry demonstrates clusters of Iba-positive cells within pneumonic tissues. **b** Flow cytometry demonstrates a higher percentage of myeloid cells and CD11b + cells (macrophages, phagocytes) in males ($n=5$), than females ($n=5$). Data represented as median ± interquartile range.

Conclusion

Our findings demonstrate that [124]I-iodo-DPA-713 accumulates within lung lesions in a hamster model of SARS-CoV-2 infection. Subtle differences between the host response of males and females can be quantified by using an unbiased CT lung segmentation tool as well as by [124]I-iodo-DPA-713 PET. This study provides proof of concept for the application of specific noninvasive biomarkers to image SARS-CoV-2-associated pulmonary inflammation. Novel molecular imaging agents could provide new insights into the pathophysiology of COVID-19, expedite the development and clinical translation of novel therapeutics against COVID-19, and also serve as clinically translatable tools for patient care.

Supplementary Information The online version contains supplementary material available at https://doi.org/10.1007/s11307-021-01638-5.

Declarations

Conflict of Interest Ali Ghayoor works at Invicro, Boston, MA, USA. A. A. O. receives consulting fees from Cubresa Inc. S. K. J. is a Senior Editor for Molecular Imaging and Biology.

References

1. Ordonez AA, Sellmyer MA, Gowrishankar G, et al (2019) Molecular imaging of bacterial infections: overcoming the barriers to clinical translation. Sci Transl Med 11

2. Scully EP, Haverfield J, Ursin RL, Tannenbaum C, Klein SL (2020) Considering how biological sex impacts immune responses and COVID-19 outcomes. Nat Rev Immunol 1–6

3. Schulte-Schrepping J, Reusch N, Paclik D et al (2020) Severe COVID-19 is marked by a dysregulated myeloid cell compartment. Cell 182:1419-+

4. GlobalHealth5050 The sex, gender and COVID-19 Project. https:// globalhealth5050.org/the-sex-gender-and-covid-19-project/ (accessed Dec 28, 2020)

5. Peckham H, de Gruijter NM, Raine C et al (2020) Male sex identified by global COVID-19 meta-analysis as a risk factor for death and ITU admission. Nat Commun 11:6317

6. Awulachew E, Diriba K, Anja A, Getu E, Belayneh F (2020) Computed tomography (CT) imaging features of patients with COVID-19: systematic review and meta-analysis. Radiol Res Pract 2020:1023506

7. Imai M, Iwatsuki-Horimoto K, Hatta M et al (2020) Syrian hamsters as a small animal model for SARS-CoV-2 infection and countermeasure development. P Natl Acad Sci USA 117:16587–16595

8. Carsana L, Sonzogni A, Nasr A et al (2020) Pulmonary post-mortem findings in a series of COVID-19 cases from northern Italy: a two-centre descriptive study. Lancet Infect Dis 20:1135–1140

9. Dhakal S, Ruiz-Bedoya CA, Zhou R, et al (2021) Sex differences in lung imaging and SARS-CoV-2 antibody responses in a COVID-19 golden Syrian hamster model. mBio:e0097421

10. Sanchez-Bautista J, Foss CA, Ordonez AA, Klunk MH, Jain SK (2019) Imaging pulmonary foreign body reaction using [I-125]iodo-DPA-713 SPECT/CT in mice. Mol Imaging Biol 21:228–231

11. Foss CA, Plyku D, Ordonez AA et al (2018) Biodistribution and radiation dosimetry of (124)I-DPA-713, a PET radiotracer for macrophage-associated inflammation. J Nucl Med 59:1751–1756

12. Ordonez AA, Pokkali S, DeMarco VP et al (2015) Radioiodinated DPA-713 imaging correlates with bactericidal activity of tuberculosis treatments in mice. Antimicrob Agents Chemother 59:642–649

13. Ordonez AA, Wintaco LM, Mota F, et al (2021) Imaging Enterobacterales infections in patients using pathogen-specific positron emission tomography. Sci Transl Med

14. Ordonez AA, Wang H, Magombedze G et al (2020) Dynamic imaging in patients with tuberculosis reveals heterogeneous drug exposures in pulmonary lesions. Nat Med 26:529–534

15. Tucker EW, Guglieri-Lopez B, Ordonez AA, et al (2018) Noninvasive (11)C-rifampin positron emission tomography reveals drug biodistribution in tuberculous meningitis. Sci Transl Med 10

16. Hesterman J, Ghayoor A, Novicki A et al (2019) Multi-atlas approaches for image segmentation across modality, species and application area. Future 6:7

17. Wang X, Ghayoor A, Novicki A, Holmes S, Seibyl J, Hesterman J (2017) Application of multi-atlas segmentation tool to hippocampus, ventricle and whole brain segmentation. Alzheimers Dement 13:P79–P80

18. Jean Philippe T (1996) Non-rigid matching using demons [abstract]. 245P

19. Wang H, Suh JW, Das SR, Pluta JB, Craige C, Yushkevich PA (2012) Multi-atlas segmentation with joint label fusion. IEEE Trans Pattern Anal Mach Intell 35:611–623

20. Foss CA, Harper JS, Wang H, Pomper MG, Jain SK (2013) Noninvasive molecular imaging of tuberculosis-associated inflammation with radioiodinated DPA-713. J Infect Dis 208:2067–2074

21. Boudewijns R, Thibaut HJ, Kaptein SJ et al (2020) STAT2 signaling restricts viral dissemination but drives severe pneumonia in SARS-CoV-2 infected hamsters. Nat Commun 11:1–10

22. Skerry C, Harper J, Klunk M, Bishai WR, Jain SK (2012) Adjunctive TNF inhibition with standard treatment enhances bacterial clearance in a murine model of necrotic TB granulomas. PLoS ONE 7:e39680

23. Hammerbeck CD, Hooper JW (2011) T cells are not required for pathogenesis in the Syrian hamster model of hantavirus pulmonary syndrome. J Virol 85:9929–9944

24. Klein SL, Pekosz A, Park HS et al (2020) Sex, age, and hospitalization drive antibody responses in a COVID-19 convalescent plasma donor population. J Clin Invest 130:6141–6150

25. Gruber AD, Osterrieder N, Bertzbach LD et al (2020) Standardization of reporting criteria for lung pathology in SARS-CoV-2–infected hamsters: what matters? Am J Respir Cell Mol Biol 63:856–859

26. Tucker EW, Pokkali S, Zhang Z et al (2016) Microglia activation in a pediatric rabbit model of tuberculous meningitis. Dis Model Mech 9:1497–1506

27. Mota F, Ordonez AA, Firth G, Ruiz-Bedoya CA, Ma MT, Jain SK (2020) Radiotracer development for bacterial imaging. J Med Chem 63:1964–1977

28. Liao M, Liu Y, Yuan J et al (2020) Single-cell landscape of bronchoalveolar immune cells in patients with COVID-19. Nat Med 26:842–844

29. Merad M, Martin JC (2020) Pathological inflammation in patients with COVID-19: a key role for monocytes and macrophages. Nat Rev Immunol 20:355–362

30. D'Alessio FR, Heller NM (2020) COVID-19 and myeloid cells: complex interplay correlates with lung severity. J Clin Investig 130

31. Klein SL (2012) Sex influences immune responses to viruses, and efficacy of prophylaxis and treatments for viral diseases. BioEssays 34:1050–1059

32. Bunders MJ, Altfeld M (2020) Implications of sex differences in immunity for SARS-CoV-2 pathogenesis and design of therapeutic interventions. Immunity

33. Klein SL, Flanagan KL (2016) Sex differences in immune responses. Nat Rev Immunol 16:626–638

34. Moradi B, Ghanaati H, Kazemi MA et al (2020) Implications of sex difference in CT scan findings and outcome of patients with COVID-19 pneumonia. Radiology: Cardiothoracic Imaging 2:e200248

35. Dangis A, De Brucker N, Heremans A et al (2020) Impact of gender on extent of lung injury in COVID-19. Clin Radiol 75:554–556

36. Shang Y, Xu C, Jiang F et al (2020) Clinical characteristics and changes of chest CT features in 307 patients with common COVID-19 pneumonia infected SARS-CoV-2: a multicenter study in Jiangsu, China. Int J Infect Dis 96:157–162

37. Spagnolo PA, Manson JE, Joffe H (2020) Sex and gender differences in health: what the COVID-19 pandemic can teach us. American College of Physicians

38. Chen T, Wu D, Chen H, et al (2020) Clinical characteristics of 113 deceased patients with coronavirus disease 2019: retrospective study. bmj 368

39. Jin S, An H, Zhou T et al (2021) Sex-and age-specific clinical and immunological features of coronavirus disease 2019. PLoS Pathog 17:e1009420

40. Salehi S, Abedi A, Balakrishnan S, Gholamrezanezhad A (2020) Coronavirus disease 2019 (COVID-19): a systematic review of imaging findings in 919 patients. AJR Am J Roentgenol 215:87–93

41. Wang Y, Dong C, Hu Y et al (2020) Temporal changes of CT findings in 90 patients with COVID-19 pneumonia: a longitudinal study. Radiology 296:E55–E64

42. Mei X, Lee H-C, Diao K-y et al (2020) Artificial intelligence–enabled rapid diagnosis of patients with COVID-19. Nat Med 26:1224–1228

43. Gieraerts C, Dangis A, Janssen L et al (2020) Prognostic value and reproducibility of AI-assisted analysis of lung involvement in COVID-19 on low-dose submillisievert chest CT: sample size implications for clinical trials. Radiology: Cardiothoracic Imaging 2:e200441

44. Kaptein SJ, Jacobs S, Langendries L et al (2020) Favipiravir at high doses has potent antiviral activity in SARS-CoV-2− infected hamsters,

whereas hydroxychloroquine lacks activity. Proc Natl Acad Sci 117:26955–26965

45. Goldstein RH (1982) Response of the aging hamster lung to elastase injury. Am Rev Respir Dis 125:295–298

46. Foss CA, Bedja D, Mease RC et al (2015) Molecular imaging of inflammation in the ApoE -/- mouse model of atherosclerosis with IodoDPA. Biochem Biophys Res Commun 461:70–75

47. Foss CA, Liu L, Mease RC, Wang H, Pasricha P, Pomper MG (2017) Imaging macrophage accumulation in a murine model of chronic pancreatitis with (125)I-Iodo-DPA-713 SPECT/CT. J Nucl Med 58:1685–1690

48. Takahashi T, Wong P, Ellingson MK, et al (2020) Sex differences in immune responses to SARS-CoV-2 that underlie disease outcomes. Nature

Publisher's Note Springer Nature remains neutral with regard to jurisdictional claims in published maps and institutional affiliations.